# Triboelectric Active Sensor Array for Self-Powered Static and Dynamic Pressure Detection and Tactile Imaging

**Long Lin,[†,§] Yannan Xie,[†,§] Sihong Wang,[†,§] Wenzhuo Wu,[†] Simiao Niu,[†] Xiaonan Wen,[†] and Zhong Lin Wang[†,‡,*]**

[†]School of Materials Science and Engineering, Georgia Institute of Technology, Atlanta, Georgia 30332-0245, United States and [‡]Beijing Institute of Nanoenergy and Nanosystems, Chinese Academy of Sciences, Beijing, China. [§]L. Lin, Y. Xie, and S. Wang contributed equally to this work.

**ABSTRACT** We report an innovative, large-area, and self-powered pressure mapping approach based on the triboelectric effect, which converts the mechanical stimuli into electrical output signals. The working mechanism of the triboelectric active sensor (TEAS) was theoretically studied by both analytical method and numerical calculation to gain an intuitive understanding of the relationship between the applied pressure and the responsive signals. Relying on the unique pressure response characteristics of the open-circuit voltage and short-circuit current, we realize both static and dynamic pressure sensing on a single device for the first time. A series of comprehensive investigations were carried out to characterize the performance of the TEAS, and high sensitivity (0.31 kPa$^{-1}$), ultrafast response time (<5 ms), long-term stability (30 000 cycles), as well as low detection limit (2.1 Pa) were achieved. The pressure measurement range of the TEAS was adjustable, which means both gentle pressure detection and large-scale pressure sensing were enabled. Through integrating multiple TEAS units into a sensor array, the as-fabricated TEAS matrix was capable of monitoring and mapping the local pressure distribution applied on the device with distinguishable spatial profiles. This work presents a technique for tactile imaging and progress toward practical applications of nanogenerators, providing potential solutions for accomplishment of artificial skin, human-electronic interfacing, and self-powered systems.

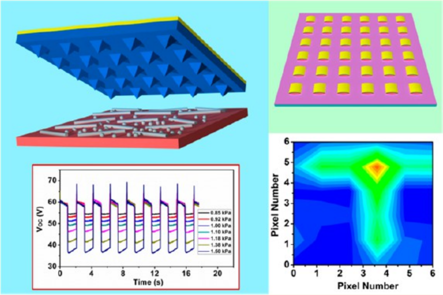

**KEYWORDS:** active sensor · triboelectric effect · nanogenerator · pressure mapping · self-powered system

Tactile sensing/imaging has been an important area of research for its applications in artificial skin,[1,2] flexible electronics,[3] human–electronics interfacing,[4] and micro-electromechanical systems (MEMS).[5] Major research efforts have been focused on improving the sensitivity, spatial resolution, response time, long-time stability, and cyclic reliability of the pressure sensor devices and the integrated matrix.[6–9] The sensing capability of most of the established pressure sensors were enabled by the pressure-induced variations of their inner properties, such as conductance,[6] capacitance,[9,10] or even optical transmittance[11] of the media (like pressure-sensitive rubbers) assisted by field effect transistors (FETs) as the read-out elements.[1,3] Employing the state-of-art micro/nanoscale fabrication and integration technology,[12–14] numerous advancements have been achieved through building a matrix of nanodevices on flexible/transparent substrates for high-resolution shape-adaptive pressure imaging.[8] But one common limitation is that most of these sensors rely on an externally supplied power source, otherwise none of them will work.

To solve this problem, the piezoelectric nanogenerator (NG)[15,16] based sensor was introduced by converting the mechanical inputs into electrical output signals without applying an external power source, which is referred as a self-powered active sensor.[17] Many potential applications have been demonstrated including wind speed detection,[18] transportation monitoring,[19] and self-powered balance,[20] *etc*. Most recently, the triboelectric nanogenerator (TENG)[21] has been invented as a promising energy conversion approach for sustainably and continuously driving personal electronics.[22,23] The working mechanism of the TENG is based on the coupling effect of contact electrification and electrostatic induction.[24–26] Both contact and sliding mode TENGs have been invented for energy harvesting from almost

* Address correspondence to zlwang@gatech.edu.

Received for review July 21, 2013 and accepted August 14, 2013.

10.1021/nn4037514

any type of mechanical energy sources,[27,28] but limited work has been demonstrated of using TENG as a self-powered pressure sensor,[29] especially in a quantitative way.

Here in this work, we fabricated a flexible triboelectric active sensor (TEAS) with excellent performance and low processing cost. The working principle of the TEAS is similar to the TENGs and was theoretically verified by numerical calculations with finite element method (FEM). Both static and dynamic pressure sensing were accomplished by the same device with different measurement approaches. Specifically, the open-circuit voltage as well as the amount of the transferred charge density was employed for static pressure detection, while the pulse-like short-circuit current peak was used for dynamic pressure monitoring. Because of this active sensing principle, a supreme performance of pressure detection was achieved on the TEAS, including high sensitivity of 0.31 kPa$^{-1}$, fast response/relaxation time of <5 ms, long-term stability/reliability of 30 000 cycles, as well as a low detection limit of 2.1 Pa. Multiple TEAS devices were integrated into a sensor array for tactile imaging, and distinguishable spatial profiles of the sensor array were realized for self-powered monitoring and mapping the applied local pressures distributions. This work is an unprecedented progress toward the practical application of nanogenerators, the realization of self-powered system, and further advancement of flexible electronic devices.

## RESULTS AND DISCUSSIONS

The device structure of the TEAS was schematically depicted in Figure 1a. On the basis of the metal–insulator triboelectric pairs, the fabrication of the TEAS device could be divided into two parts. In the first part, the polydimethylsiloxane (PDMS) membrane was modified with micropatterned pyramid structures through photolithography and template method (Figure S1, Supporting Information (SI)). A scanning electron microscopy (SEM) image of its surface morphology is shown in Figure 1b. The pyramid microstructures were uniformly distributed on the inner surface of PDMS, with the size of ~10 $\mu$m. The processed PDMS membrane was deposited with Au electrode on its outer surface. In the second part, a piece of Al was assembled with the composite of Ag nanowires and nanoparticles that were prepared by a seed-mediated approach.[30] The micro/nanostructures on both inner surfaces were introduced to enhance the triboelectric effect and the effective contact area between the two surfaces, which would help to improve the pressure response of the TEAS. The two layers were bonded by nonconductive tapes, and both electrodes were connected to electrical leads. Because of the elastic resilience of the materials, the device naturally forms an arch shape, with an air gap presented for effective charge separation (inset of Figure 1a). The size of the TEAS is 2 × 2 cm, which of course can be much reduced in size.

The typical electrical responses of the TEAS under external agitations by a mechanical shaker (ET-126-1-4, Labworks, Inc.) are shown in Figure 1d–f. With a 2 Hz cyclic pressing force applied on the TEAS, it produces an open-circuit voltage ($V_{OC}$) of ~75 V, transferred charge density ($\Delta\sigma$) of ~45 $\mu$C/m$^2$, and short-circuit current density ($J_{SC}$) of ~3 mA/m$^2$. The working principle of the TEAS is based on the coupling effect of contact electrification and electrostatic induction. When the two triboelectric layers are brought into contact by an external force/pressure, the electrons will be injected from the Al layer into the PDMS layer (due to the difference in ability to attract electrons), leaving net positive charges in Al foil and net negative charges on the surface of the PDMS membrane. In the open-circuit (OC) condition, as the external pressure is withdrawn, the $V_{OC}$ will increase linearly corresponding to the vertical gap distance between the two layers ($d$) *via* the following equation:

$$V_{OC} = \frac{\sigma \cdot d}{\varepsilon_0} \qquad (1)$$

where $\varepsilon_0$ is the permittivity in vacuum and $\sigma$ is the triboelectric charge density, which is considered as constant in this work. It should be noted that the $V_{OC}$ starts decreasing when the external pressure is applied (with smaller $d$) and reverts to its maximum level when the pressure is fully removed ($d = d_0$). As for the short-circuit (SC) condition, this change of potential difference in correspondence to the mechanical agitation will drive the electrons moving back and forth in the external circuit, leading to a current flow with AC manner. The amount of the transferred charge density ($\Delta\sigma$) as a result of pressure change is also a function of $d$, which is given by the following:

$$\Delta\sigma = \frac{Q_0 - Q}{S} = \frac{\sigma \cdot d_0}{\frac{d_{PDMS}}{\varepsilon_{r,\,PDMS}} + d_0} - \frac{\sigma \cdot d}{\frac{d_{PDMS}}{\varepsilon_{r,\,PDMS}} + d} \qquad (2)$$

where $Q$ and $Q_0$ are the amount of induced charges on one electrode with and without pressure, respectively, $S$ is the effective area of electrodes, $d_{PDMS}$ and $\varepsilon_{r,PDMS}$ are the thickness and relative dielectric constant of the PDMS membrane, respectively, and $d_0$ is the maximum gap distance without pressure. Apparently, the $\Delta\sigma$ increases as $d$ is reduced, but not with linear relationship. Hence, the $J_{SC}$ could be deducted as

$$J_{SC} = \frac{d(\Delta\sigma)}{dt} = -\frac{dQ}{S \cdot dt} = \frac{\sigma \cdot \frac{d_{PDMS}}{\varepsilon_{r,\,PDMS}}}{\left(\frac{d_{PDMS}}{\varepsilon_{r,\,PDMS}} + d\right)^2} \cdot \frac{\delta d}{\delta t} \qquad (3)$$

It can be found that the magnitude of the $J_{SC}$ is not only dependent on the gap distance but also affected by the loading rate of the external pressure ($\delta d/\delta t$).

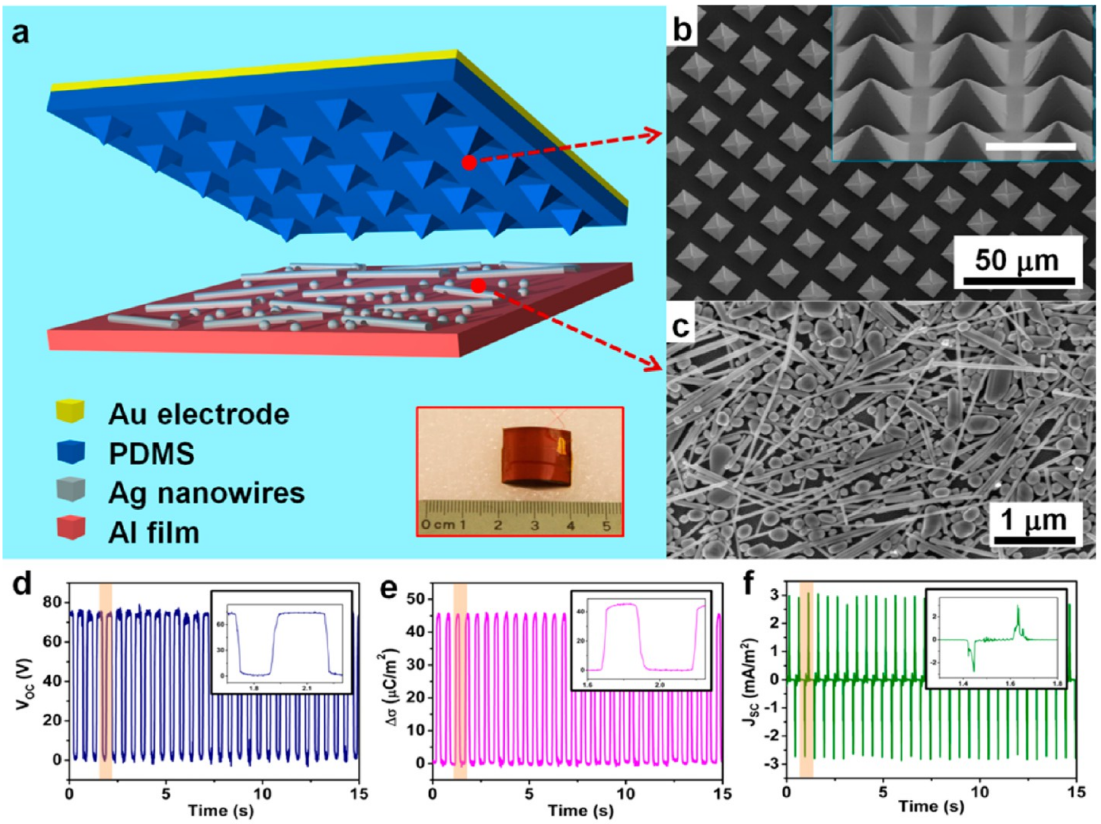

Figure 1. The basic structure and typical electrical response of the triboelectric active sensor applied with a cyclic pressure. (a) The schematic illustration of the TEAS device with both inner surfaces modified by micropattern PDMS structures and Ag nanowires/nanoparticles composite. The inset is a photograph of the TEAS device. (b) The SEM image of the pyramid-structured micropatterns fabricated on the inner surface of the PDMS membrane. The inset is a high magnification SEM image of the micropatterns, and the inset scale bar is 10 $\mu$m. (c) The SEM image of the Ag nanowires/nanoparticles composite assembled on the inner surface of the Al foil. (d,e) The measured typical electrical response including (d) the open-circuit voltage, (e) the transferred charge density, and (f) the short-circuit current density of the TEAS upon a cyclic pressure.

This expectation was confirmed in the measurement with higher frequency of the applied pressure (6 Hz), and the $J_{SC}$ displays a gigantic increase up to ~40 mA/m$^2$ (Figure S2 (SI)).

Therefore, the output open-circuit signal from the TEAS (see eq 1) is a static signal that is only dictated by the gap distance $d$, which is a measure of the magnitude of the applied pressure/force. The output current eq 3 is a dynamic signal that is determined by the speed at which the gap was squeezed; thus, it gives the information about the rate of the pressure/force being applied.

Continuing from the above analysis, the $V_{OC}$ has direct and linear relationship with $d$, and thus will be an ideal parameter for static pressure measurement. Therefore, a numerical calculation regarding to the $V_{OC}-d$ relationship is necessary to verify the theoretical basis of the TEAS. For simplicity purposes, the TEAS device is treated as parallel-plate capacitor in the established model, where the PDMS plate with Au electrode was placed parallel with the Al plate with variable gap distances ranging from 0 to 20 $\mu$m. The triboelectric charge density on the inner surface of PDMS plate was assigned as 45 $\mu$C/m$^2$, which is equal to the measured transferred charge density in Figure 1e. The calculated potential distribution around the parallel-plate structure is displayed with color scaling in Figure 2a–e. It can be found that the potential difference between the top and bottom electrodes shows an obvious decreasing trend with decreasing gap distance (increasing pressure). The potential difference decreases to 0 when the two plates reach a full contact (Figure 2e, $d$ = 0), as expected from eq 1. The calculated potential difference displays perfect linear relationship with the gap distance and very little deviation from the proposed relationship in eq 1 (Figure 2f). Moreover, the calculation was also conducted with different device sizes (5, 2, and 1 mm in plate width), as summarized in Figure S3 (SI). Little difference could be observed from the list of calculation results, indicating that the edge effect could be excluded on condition that the size of the device far surpasses the gap distance.

In order to correlate the external pressure with the $V_{OC}$, the material resilience of the TEAS was considered as the spring-entangled structure using the Hooker's Law:

$$p = \frac{k \cdot x}{S} = \frac{k \cdot (d_0 - d)}{S} \qquad (4)$$

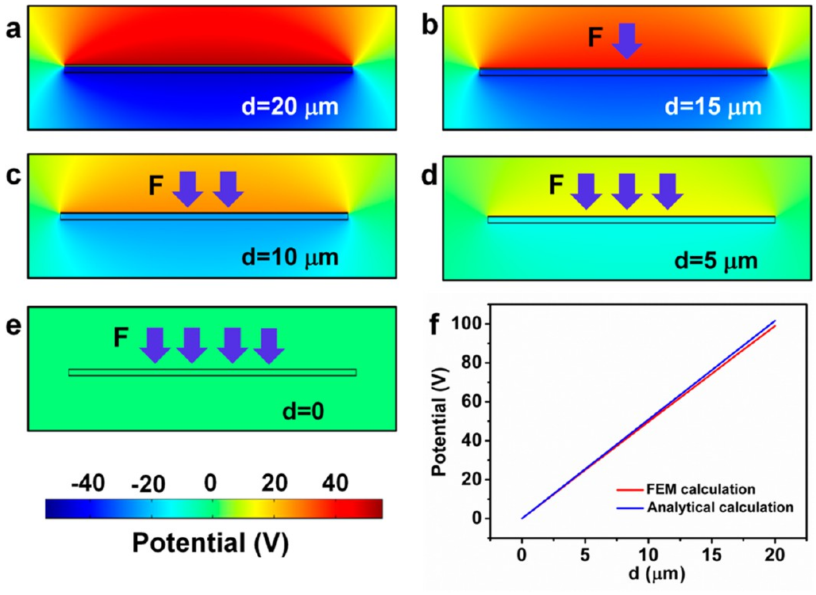

**Figure 2. Numerical calculations of the correlation between the potential difference and the gap distance of the TEAS. (a−e) The calculated potential distributions around the TEAS with variable gap distances ranging from (a) 20, (b) 15, (c) 10, (d) 5, and (e) 0 μm. The bottom inset is the color scale of the potential. (f) The summarized calculation results indicating the relationship between the potential difference and the gap distance, as well as the comparison of the calculation results *via* the finite element method and the analytical formula.**

where $p$ is the pressure and $k$ represents the elastic property of the materials in the TEAS. Combining eq 1 and 4, we can get

$$\frac{V_{OC,0}-V_{OC}}{V_{OC,0}} = \frac{d_0-d}{d_0} = \frac{S}{k\cdot d_0}\cdot p \qquad (5)$$

Hence the relative variation of the $V_{OC}$ should be expected to show a directly linear relationship with the applied pressure, and thus it is a reliable parameter for measuring the magnitude of the external pressure applied onto the TEAS, while the $J_{SC}$ is able to provide the dynamic information of the applied pressure (*i.e.*, loading rate). Combining the analysis on the measurement of both the $V_{OC}$ and the $J_{SC}$, the TEAS device is capable of giving the detailed information about the ambient mechanical stimulations. On this basis, we designed and conducted a series of measurements to characterize the performance of the TEAS, as discussed below.

The schematic illustration of the measurement setup for the TEAS is sketched in Figure S4 (SI). The TEAS device was attached onto a flat plate and fixed on the end of a force gauge (Vernier Software & Technology), and cyclic external pressures were applied by a mechanical linear motor. The data for both the output parameters (the $V_{OC}$, $\Delta\sigma$, and $J_{SC}$) and the real-time force/pressure were recorded and analyzed in the same computer. Figure 3a is the real-time measurement result of $V_{OC}$ under series of different pressures. The reference level of voltage was selected in the way that the $V_{OC}$ approached 0 with the maximum pressure when the two surfaces came into full contact. It could be observed that the $V_{OC}$ stays at the maximum level ($V_0 = 60$ V) when there is no pressure, and decreases to a lower level once the external pressure is applied. The voltage variation ($V_0 - V$) increases with increasing pressure, and the relationship between relative voltage variation ($V_0 - V$)/$V_0$ and magnitude of pressure is plotted in Figure 3b (the subscript "OC" is omitted here for convenient expression). The plot can be divided into two regions based on difference in sensitivity. In the low pressure region (Region I), the sensitivity of the TEAS is 0.31 kPa$^{-1}$, which is much higher than that of the high pressure region (0.01 kPa$^{-1}$ in Region II). The separated fittings of the data in both regions display good linear behavior ($R_I^2 = 0.965$, and $R_{II}^2 = 0.985$), which reveals the validity of the device as a reliable pressure sensor. The reason for different sensitivities can be explained on the basis of the previous analysis. In Region I, the pressure increase results in drastic gap distance change as estimated in eq 4, introducing larger voltage variations, while it is quite probable that the gap distance has already been close to 0 from the turning point in Region II, and the increasing pressure only works for enhancing the effective contact area between the two layers. In other words, the $V_{OC}$ tends to saturate to zero in Region II, and the applied pressure has little effect on the voltage variation.

To verify the theoretical expectation that the $V_{OC}$ merely depends on the magnitude of the applied pressure rather than the loading rate, the voltage response of the TEAS was tested at a constant pressure of ~2 kPa but of different loading rates that were controlled by the accelerations of the linear motor. As shown in Figure 3c,d, as the accelerations vary from 2.5 to 30 m/s$^2$, the relative voltage variations almost remain constant, though a minor increasing trend is

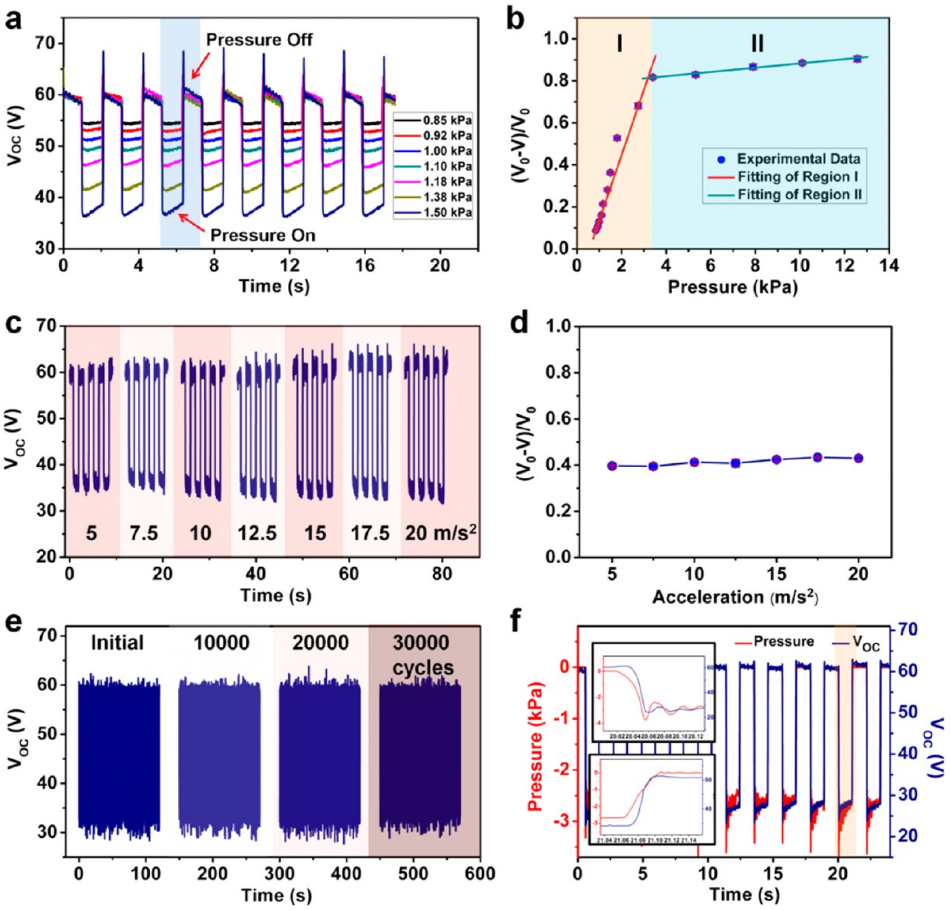

**Figure 3. The static pressure sensing of the TEAS through measurement of the open-circuit voltage. (a) The real-time measurement of the $V_{OC}$ with cyclic and variable pressures applied on the TEAS device. The highlighted region indicates one cycle of the pressure loading and unloading process. (b) The summarized relationship and linear fitting between the relative variations of voltage and the pressure applied on the TEAS device. (c) The measurement of the $V_{OC}$ with a cyclic and constant pressure (2 kPa) applied on the TEAS with variable accelerations. (d) The summarized relationship between the relative voltage variations and accelerations. (e) The stability test for static pressure sensing of the TEAS with continuous loading and unloading a cyclic pressure (2.5 kPa) for 30 000 cycles. The $V_{OC}$ was measured after each 10 000 cycles, and 300 cycles of data were recorded and presented in the plot. (f) The comparison of the real-time measurement of both the applied pressure (red curve) and the $V_{OC}$ (blue curve). The top inset and bottom inset are the enlarged view of the loading and unloading process in the highlighted cycle, respectively. The response/relaxation times are <5 ms from the time interval of the two curves.**

present, possibly resulting from minor pressure variations. The stability of the TEAS device was examined through continuously loading and unloading a constant pressure (~ 2.5 kPa) for over 30 000 cycles, as exhibited in Figure 3e. The voltage response was measured after every 10 000 cycles, during which 300 cycles were recorded and displayed in Figure 3e. The voltage response only shows a minor decay of ~6.7% after 30 000 cycles, through which the stability of the TEAS is confirmed. Moreover, in Figure 3f, the real-time pressure measurement and voltage response was displayed in the same plot, and both plots match perfectly. Hence, the voltage response is capable of revealing the detailed information of the loading process of an external pressure. From the comparison of plots for the loading and unloading process of the external pressure, it is estimated that both the response time and the relaxation time are <5 ms, demonstrating the prompt response of the nanogenerator-based active pressure sensor and proving its superior advantage to conventional sensors.

Furthermore, besides the $V_{OC}$, the $\Delta\sigma$ was also a reliable parameter that could be used for static pressure sensing. In this aspect, the similar measurements were then carried out with variable pressures loaded on the TEAS device, and the data of the $\Delta\sigma$ was recorded and displayed in the same way (Figure S5 (SI)). Different from the $V_{OC}$, the $\Delta\sigma$ is 0 without pressure and increases as the applied pressure is elevated. Similarly, the relationship of the $\Delta\sigma$ with increasing pressure also has two different sensitivity regions: a high sensitivity region at lower pressures and a drastically decreased sensitivity at higher pressures. The acceleration dependence at constant loading pressure was measured, and the amount of $\Delta\sigma$ also keeps constant with variable accelerations of the linear motor, though small variation exists. The stability of this type of measurement was confirmed by continuously loading and unloading a constant pressure of 2.5 kPa for 30 000 cycles, as shown in Figure S6 (SI).

Different from the $V_{OC}$ and the $\Delta\sigma$, the $J_{SC}$ is not only dependent on the applied force/pressure, but also related to the loading rate of the external force, as discussed in eq 3 above. Furthermore, the output profile of the $J_{SC}$ is a pulse-like current peak, which enables its application for dynamic pressure detection. On the basis of this expectation, both the effect of the force/pressure magnitude and the acceleration were tested on the TEAS for peak current measurement. The measured rectified $J_{SC}$ with variable pressures under the same loading rate were displayed in Figure 4a, showing a clearly increasing trend with elevated pressures. The full data summarized in Figure 4b shows the reversibility of the current response. The loading pressure was first increased from low pressure region (<1 kPa) to a high pressure region (∼ 9 kPa) and then decreased to the original magnitude. The resulting current response in the decreasing-pressure curve does not exhibit much deviation in reference to the original curve, thus demonstrating the reliability of the current measurement. Similarly, the current response with a constant pressure (0.75 kPa) and variable accelerations was measured and shown in Figure 4c,d. The peak values of the output $J_{SC}$ also have positive correlation with the acceleration of the applied pressure. Both the relationship between the peak value of the $J_{SC}$ and the applied pressure/acceleration could be explained using eq 3, where the loading rate $\delta d/\delta t$ is positively related to the acceleration of the linear motor. Therefore, with increasing applied pressure or acceleration, the term $d$ will decrease or $\delta d/\delta t$ will increase, both leading to the enhancement of the absolute value of the $J_{SC}$.

Furthermore, the cycling stability test of the rectified $J_{SC}$ under continuous pressure triggering for 30 000 cycles was carried out in the same way as the test of the $V_{OC}$, and little decay could be found in the measurement results (Figure 4e). In addition, the dynamic reliability of the TEAS was further confirmed by recording the peak current response with variable pressures after every 10 000 triggering cycles. The results shown in Figure 4f also demonstrate that the measured $J_{SC}$-pressure relationship after continuous triggering is close to the original test. More impressively, the dynamic pressure sensing limit of the TEAS was examined by comparing the output signals of both a gentle pressure (0.125 kPa) and the corresponding noise level, as shown in Figure S7 (SI). The low-end detection limit ($p_0$) of the TEAS is then calculated by the following equation:

$$p_0 = \frac{p}{J_{SC}/J_{SC,\,\text{noise}}} = \frac{0.125}{0.15/0.0025}\ \text{kPa} = 2.1\ \text{Pa} \quad (6)$$

Thus, the low-end detection limit of the TEAS is merely 2.1 Pa, elaborating the high sensitivity of the nanogenerator as an active pressure sensor.

Above all, it could be clearly found that the high sensitivity range of the TEAS is confined within a low pressure region (<5 kPa), as both the voltage and current signal tend to get saturated when the pressure reaches a higher level. This performance might limit the practical applications of the TEAS, and the extension of higher detection range is highly desirable. In this regard, we designed a new type of TEAS with the original device entangled by a plastic bracket with elastic springs to enforce the whole structure. On the basis of this newly fabricated device, the voltage, charge transfer, and current responses of the TEAS with variable pressures were measured (Figure S8 (SI)). From the summarized results, we can find that the linear and high sensitivity region has been expanded to ∼40 kPa. The typical responses with a certain cyclic applied pressure are shown in Figure S9 (SI). With such high pressure, the response signal was also enabled to reveal the details of the applied pressure. More importantly, this pressure-extended TEAS device could be employed for sensing the applied pressure with continuously step-by-step loading and unloading process, as shown in Figure S10 (SI). These results further validate the reversibility and reliability of the TEAS device at a higher pressure range.

The array of the TEAS devices was fabricated on a flat plate with deposited Al thin film as a common electrode, as schematically illustrated in Figure 5a. The photograph of the as-fabricated TEAS array is shown in Figure S11 (SI). The unit of the array device has the same size as the single TEAS device mentioned above. Each pixel was marked the letter/number coordinates from “A1” to “F6”. The response of the TEAS array with local pressure was measured through a multichannel measurement system (National Instruments), as schematically depicted in Figure S12 (SI). The Al electrodes of all the TEAS units were connected to a common electrode on the plate with conductive paste, while the upper Au electrode of each unit was connected to the probe of each measurement channel. The measurement instrument is a voltage meter with an internal resistance of ∼10 MΩ, and a corresponding voltage peak will be recorded as response of a local pressure on the corresponding TEAS unit in the matrix. As shown in Figure S13 (SI), a quarter of pixels (Pixels A1−C3) in the array were pressed simultaneously, and the voltage peaks were only detected from Pixels A1−C3, while the output profile of the other channels remain almost unchanged in the same time period.

On the basis of this working principle, we demonstrated the tactile imaging capability of the TEAS matrix by loading pressure through predesigned plastic architecture with the calligraphy of the letters “TENG”, respectively. Before applying the pressure, the voltage outputs from all the pixels of the TEAS matrix were at the background level, as displayed in Figure 5b. Figure 5c−f shows the two-dimensional

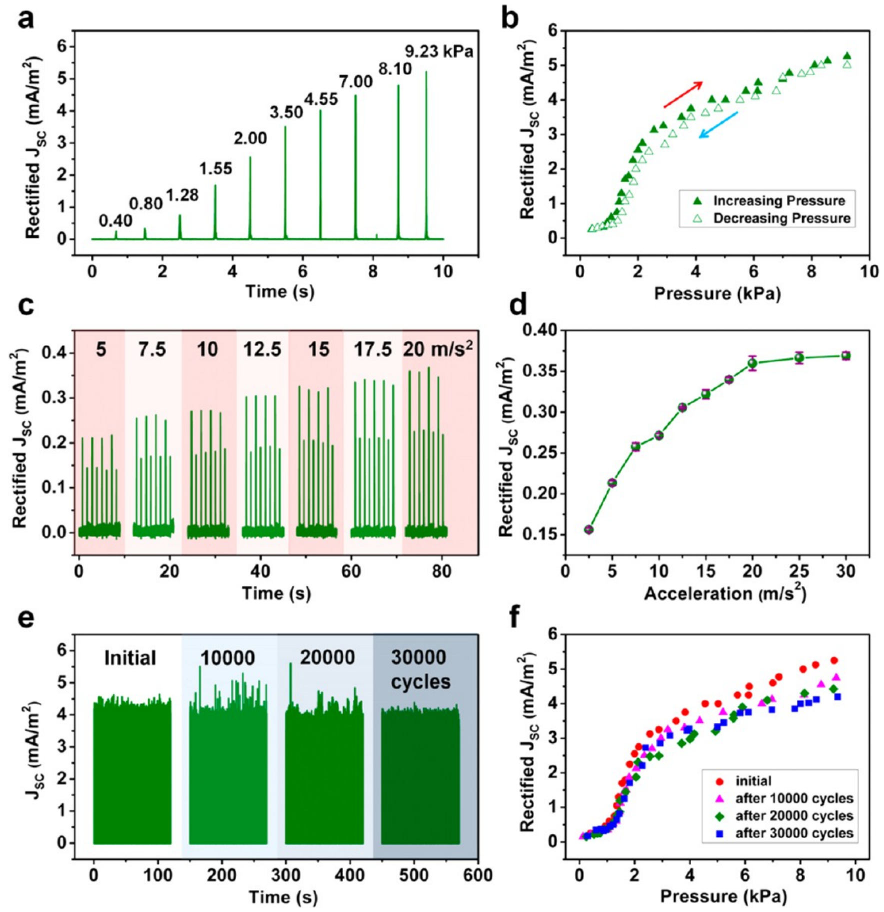

**Figure 4. Dynamic pressure sensing of the TEAS through measurement of the short-circuit current density. (a) The measured rectified pulse-like $J_{SC}$ with variable pressures applied on the TEAS device. (b) The summarized data of the rectified $J_{SC}$ with variable pressures applied on the TEAS device and the reversibility test by increasing the pressure in the first test cycle and decreasing the pressure in the second test cycle. (c) The measured rectified $J_{SC}$ with a constant pressure (0.75 kPa) applied on the TEAS device but with variable accelerations. (d) The summarized data of the rectified $J_{SC}$ with a constant pressure but with variable accelerations ranging from 2.5 to 30 m/s$^2$. (e) The stability test for dynamic pressure sensing of the TEAS with continuous loading and unloading for 30 000 cycles. The $J_{SC}$ was measured after each 10 000 cycles, and 300 cycles of data were recorded and presented in the plot. (f) The reliability test of the dynamic pressure sensing. The measurement of the rectified $J_{SC}$ with variable pressures was carried out after each 10 000 cycles and compiled in the same plot.**

contour plotting of the peak value of the voltage responses that were measured when external pressures were applied through each architecture, respectively. The highlighted color represents the area under pressing through each letter, as outlined by the white dash lines. These plots elaborate the spatial resolution of the TEAS matrix for distinguishably mapping the calligraphy of the applied pressure, and its potential applications such as personal signature recognition. In addition, to gain a more intuitive understanding of the "self-powered" pressure mapping functionality of the TEAS matrix, each nine units of the same array device were connected in parallel to power up a serially connected array of LEDs showing "T", "E", "N", "G" characters, respectively, as lively demonstrated in Video S1 (SI). This demonstration proves that the TEAS matrix can work as an external power source and a sensor array simultaneously for a truly stand-alone self-powered system.

The active pressure sensor and the integrated sensor array based on the triboelectric effect presented in this work have several advantages over conventional passive pressure sensors. First, the active sensor in this work is capable of both static pressure sensing using the open-circuit voltage and dynamic pressure sensing using the short-circuit current, while conventional sensors are usually incapable of dynamic sensing to provide the loading rate information. Second, the prompt response of both static and dynamic sensing enables the revealing of details about the loading pressure. Third, the detection limit of the TEAS for dynamic sensing is as low as 2.1 Pa, because of the high output of the TENG. Last but not least, the active sensor array presented in this work has no power consumption and could even be combined with its energy harvesting functionality for self-powered pressure mapping. Future works in this field involve the miniaturization of the pixel size to achieve higher spatial resolution, and the integration of the TEAS matrix onto fully flexible substrate for shape-adaptive pressure imaging.

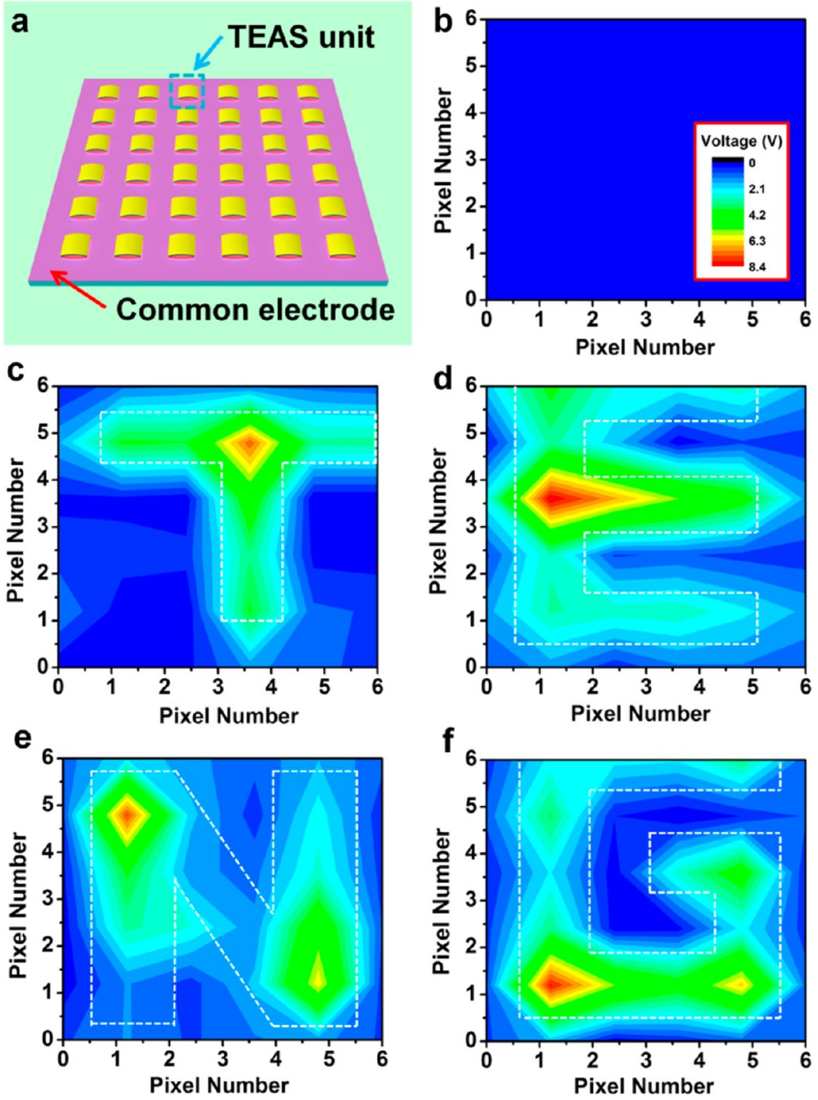

Figure 5. Self-powered pressure mapping based on the TEAS array. (a) A schematic illustration of the TEAS array device. (b) The background signal with no pressure applied on the TEAS matrix. The inset is color scaling of voltage for all the measurements in this figure. (c–f) The two-dimensional voltage contour plot from the multichannel measurement of the TEAS matrix with an external pressure uniformly and locally applied onto the device through architectures with calligraphy of "T", "E", "N", and "G", respectively.

## CONCLUSION

In summary, a self-powered, highly sensitive, and fast responsive pressure sensor was demonstrated on the basis of the triboelectric effect. The performance of the triboelectric active sensor was characterized by static sensing with the open-circuit voltage, and dynamic sensing with the short-circuit current. The long-term stability, cycling repeatability, as well as adjustable sensing range were realized because of the robustness of the active pressure sensor. Multiple triboelectric active sensors were integrated into a sensor array for self-powered pressure mapping, and spatially distinguishable tactile imaging was demonstrated. This work is a milestone progress in nanogenerator-based active sensor, which not only realizes its energy harvesting and pressure sensing functionalities at the same time, but also initiates possible applications such as personal signature recognition or electronic skins.

## EXPERIMENTAL SECTION

**Fabrication of the Triboelectric Active Sensor Device.** The fabrication process flow of the micropatterned PDMS membrane is depicted in Figure S1 (SI). Basically, the predesigned micropatterns were first transferred to the Si wafer through photolithography and wet etching; then, the PDMS elastomer and curing agent were mixed and spin-coated onto the Si mold; finally, the PDMS was cured and peeled off from the Si mold and deposited with Au electrode (Unifilm Sputter). The Ag nanowires/nanoparticles composite was synthesized by a two-step seed-mediated solution growth approach. In the first step, the Pt nanoparticles were formed through reducing $PtCl_2$ with ethylene glycol refluxed at 160 °C; then $AgNO_3$ and poly(vinyl pyrrolidone) (PVP) were added into the solution and refluxed for 40 min. Both Ag nanoparticles and nanowires formed also by reaction with ethylene glycol. The product mixtures were rinsed with acetone to remove the excess PVP for three times after centrifugation. The Al foil was immersed into the solution of the Ag nanowires/nanoparticles composite for 12 h for full absorption and then baked at 100 °C for 2 h to evaporate the liquid.

**Measurement of the Real-Time Force Applied on the TEAS Device and the Electrical Response Signals.** In the characterizations of a single TEAS device, the applied force was measured by the Dual-Range Force Sensor (Vernier Software & Technology). The $V_{OC}$ and the $\Delta\sigma$ were measured by the Kiethley 6514 electrometer, and the $J_{SC}$ was measured by the SR570 current preamplifier (Stanford Research System). The multichannel recording of the voltage response from the TEAS matrix was carried out by the digital multimeter (NI PXI-4072), and the synchronized operations among the PXI modules as well as the data acquisition controlled by the customized Labview code (National Instruments).

*Conflict of Interest:* The authors declare no competing financial interest.

*Supporting Information Available:* Additional discussions, figures, and video. This material is available free of charge *via* the Internet at http://pubs.acs.org.

*Acknowledgment.* This research was supported by MURI, U.S. Department of Energy, Office of Basic Energy Sciences (DE-FG02-07ER46394), NSF, NSFC (61176067), and the Knowledge Innovation Program of the Chinese Academy of Sciences (KJCX2-YW-M13). The authors thank Dr. Youfan Hu, Ken C. Pradel, and Qingshen Jing for technical assistance and stimulating discussions.

## REFERENCES AND NOTES

1. Someya, T.; Sekitani, T.; Iba, S.; Kato, Y.; Kawaguchi, H.; Sakurai, T. A Large-Area, Flexible Pressure Sensor Matrix with Organic Field-Effect Transistors for Artificial Skin Applications. *Proc. Natl. Acad. Sci. U. S. A.* **2004**, *101*, 9966–9970.
2. Takei, K.; Takahashi, T.; Ho, J. C.; Ko, H.; Gillies, A. G.; Leu, P. W.; Fearing, R. S.; Javey, A. Nanowire Active-Matrix Circuitry for Low-Voltage Macroscale Artificial Skin. *Nat. Mater.* **2010**, *9*, 821–826.
3. Sekitani, T.; Yokota, T.; Zschieschang, U.; Klauk, H.; Bauer, S.; Takeuchi, K.; Takamiya, M.; Sakurai, T.; Someya, T. Organic Nonvolatile Memory Transistors for Flexible Sensor Arrays. *Science* **2009**, *326*, 1516–1519.
4. Kim, D. H.; Lu, N. S.; Ma, R.; Kim, Y. S.; Kim, R. H.; Wang, S. D.; Wu, J.; Won, S. M.; Tao, H.; Islam, A.; et al. Epidermal Electronics. *Science* **2011**, *333*, 838–843.
5. Li, M.; Tang, H. X.; Roukes, M. L. Ultra-Sensitive NEMS-Based Cantilevers for Sensing, Scanned Probe and Very High-Frequency Applications. *Nat. Nanotechnol.* **2007**, *2*, 114–120.
6. Lipomi, D. J.; Vosgueritchian, M.; Tee, B. C. K.; Hellstrom, S. L.; Lee, J. A.; Fox, C. H.; Bao, Z. N. Skin-Like Pressure and Strain Sensors Based on Transparent Elastic Films of Carbon Nanotubes. *Nat. Nanotechnol.* **2011**, *6*, 788–792.
7. Tee, B. C. K.; Wang, C.; Allen, R.; Bao, Z. N. An Electrically and Mechanically Self-Healing Composite with Pressure- and Flexion-Sensitive Properties for Electronic Skin Applications. *Nat. Nanotechnol.* **2012**, *7*, 825–832.
8. Wu, W. Z.; Wen, X. N.; Wang, Z. L. Taxel-Addressable Matrix of Vertical-Nanowire Piezotronic Transistors for Active and Adaptive Tactile Imaging. *Science* **2013**, *340*, 952–957.
9. Schwartz, G.; Tee, B. C. K.; Mei, J.; Appleton, A. L.; Kim, D. H.; Wang, H.; Bao, Z. Flexible Polymer Transistors with High Pressure Sensitivity for Application in Electronic Skin and Health Monitoring. *Nat. Commun.* **2013**, *4*, 1859.
10. Mannsfeld, S. C. B.; Tee, B. C. K.; Stoltenberg, R. M.; Chen, C.; Barman, S.; Muir, B. V. O.; Sokolov, A. N.; Reese, C.; Bao, Z. N. Highly Sensitive Flexible Pressure Sensors with Microstructured Rubber Dielectric Layers. *Nat. Mater.* **2010**, *9*, 859–864.
11. Ramuz, M.; Tee, B. C. K.; Tok, J. B. H.; Bao, Z. N. Transparent, Optical, Pressure-Sensitive Artificial Skin for Large-Area Stretchable Electronics. *Adv. Mater.* **2012**, *24*, 3223–3227.
12. Zhong, Z. H.; Wang, D. L.; Cui, Y.; Bockrath, M. W.; Lieber, C. M. Nanowire Crossbar Arrays as Address Decoders for Integrated Nanosystems. *Science* **2003**, *302*, 1377–1379.
13. Javey, A.; Nam, S.; Friedman, R. S.; Yan, H.; Lieber, C. M. Layer-by-Layer Assembly of Nanowires for Three-Dimensional, Multifunctional Electronics. *Nano Lett.* **2007**, *7*, 773–777.
14. Kim, D. H.; Ahn, J. H.; Choi, W. M.; Kim, H. S.; Kim, T. H.; Song, J. Z.; Huang, Y. G. Y.; Liu, Z. J.; Lu, C.; Rogers, J. A. Stretchable and Foldable Silicon Integrated Circuits. *Science* **2008**, *320*, 507–511.
15. Wang, Z. L.; Song, J. H. Piezoelectric Nanogenerators Based on Zinc Oxide Nanowire Arrays. *Science* **2006**, *312*, 242–246.
16. Yang, R. S.; Qin, Y.; Dai, L. M.; Wang, Z. L. Power Generation with Laterally Packaged Piezoelectric Fine Wires. *Nat. Nanotechnol.* **2009**, *4*, 34–39.
17. Pan, C. F.; Li, Z. T.; Guo, W. X.; Zhu, J.; Wang, Z. L. Fiber-Based Hybrid Nanogenerators for/as Self-Powered Systems in Biological Liquid. *Angew. Chem., Int. Ed.* **2011**, *50*, 11192–11196.
18. Sun, C. L.; Shi, J.; Bayerl, D. J.; Wang, X. D. PVDF Microbelts for Harvesting Energy from Respiration. *Energy Environ. Sci.* **2011**, *4*, 4508–4512.
19. Lin, L.; Hu, Y. F.; Xu, C.; Zhang, Y.; Zhang, R.; Wen, X. N.; Wang, Z. L. Transparent Flexible Nanogenerator as Self-Powered Sensor for Transportation Monitoring. *Nano Energy* **2013**, *2*, 75–81.
20. Lin, L.; Jing, Q. S.; Zhang, Y.; Hu, Y. F.; Wang, S. H.; Bando, Y.; Han, R. P. S.; Wang, Z. L. An Elastic-Spring-Substrated Nanogenerator as an Active Sensor for Self-Powered Balance. *Energy Environ. Sci.* **2013**, *6*, 1164–1169.
21. Fan, F. R.; Tian, Z. Q.; Wang, Z. L. Flexible Triboelectric Generator!. *Nano Energy* **2012**, *1*, 328–334.
22. Wang, S. H.; Lin, L.; Wang, Z. L. Nanoscale Triboelectric-Effect-Enabled Energy Conversion for Sustainably Powering Portable Electronics. *Nano Lett.* **2012**, *12*, 6339–6346.
23. Lin, L.; Wang, S.; Xie, Y.; Jing, Q.; Niu, S.; Hu, Y.; Wang, Z. L. Segmentally Structured Disk Triboelectric Nanogenerator for Harvesting Rotational Mechanical Energy. *Nano Lett.* **2013**, *13*, 2916–2923.
24. Grzybowski, B. A.; Winkleman, A.; Wiles, J. A.; Brumer, Y.; Whitesides, G. M. Electrostatic Self-Assembly of Macroscopic Crystals Using Contact Electrification. *Nat. Mater.* **2003**, *2*, 241–245.
25. Zhu, G.; Pan, C. F.; Guo, W. X.; Chen, C. Y.; Zhou, Y. S.; Yu, R. M.; Wang, Z. L. Triboelectric-Generator-Driven Pulse Electrodeposition for Micropatterning. *Nano Lett.* **2012**, *12*, 4960–4965.
26. Diaz, A. F.; Felix-Navarro, R. M. A Semi-Quantitative Triboelectric Series for Polymeric Materials: The Influence of Chemical Structure and Properties. *J. Electrost.* **2004**, *62*, 277–290.
27. Zhu, G.; Lin, Z. H.; Jing, Q. S.; Bai, P.; Pan, C. F.; Yang, Y.; Zhou, Y. S.; Wang, Z. L. Toward Large-Scale Energy Harvesting by a Nanoparticle-Enhanced Triboelectric Nanogenerator. *Nano Lett.* **2013**, *13*, 847–853.
28. Wang, S.; Lin, L.; Xie, Y.; Jing, Q.; Niu, S.; Wang, Z. L. Sliding-Triboelectric Nanogenerators Based on In-Plane Charge-Separation Mechanism. *Nano Lett.* **2013**, *13*, 2226–2233.
29. Fan, F. R.; Lin, L.; Zhu, G.; Wu, W. Z.; Zhang, R.; Wang, Z. L. Transparent Triboelectric Nanogenerators and Self-Powered Pressure Sensors Based on Micropatterned Plastic Films. *Nano Lett.* **2012**, *12*, 3109–3114.
30. Sun, Y. G.; Gates, B.; Mayers, B.; Xia, Y. N. Crystalline Silver Nanowires by Soft Solution Processing. *Nano Lett.* **2002**, *2*, 165–168.